

High Resolution Element Mapping Inside Biological Samples using Fluorescence Microtomography

Christian G. Schroer^a, Boris Benner^a, Til Florian Günzler^a,
Marion Kuhlmann^a, Bruno Lengeler^a, Walter H. Schröder^b, Arnd J. Kuhn^b,
Alexandre S. Simionovici^c, Anatoly Snigirev^c, Irina Snigireva^c

^aII. Physikalisches Institut, Aachen University of Technology RWTH,
D-52056 Aachen, Germany

^bIBI 1, Forschungszentrum Jülich, D-52425 Jülich, Germany

^cEuropean Synchrotron Radiation Facility (ESRF), B.P. 220,
F-39043 Grenoble CEDEX, France

ABSTRACT

Sample preparation for element analysis of many biological tissues is difficult to achieve and prone to introduce contamination. Using x-ray fluorescence element microtomography (XFEMT) the element distribution on a virtual section across the sample can be determined with a resolution in the micrometer range. Fluorescence microtomograms of two plant samples are shown, demonstrating the possibility to map physiologically relevant ions, trace elements, and heavy metal pollutants at the cellular level. Attenuation effects inside the plant are corrected by a self-consistent tomographic reconstruction technique.

Keywords: fluorescence analysis, tomography, x-ray microbeam, compound refractive lenses

1. INTRODUCTION

Element analysis using X-ray fluorescence excited by monochromatic synchrotron radiation is a powerful tool with high sensitivity and low detection limits. Combining x-ray fluorescence with scanning microprobe techniques allows to study element distributions in inhomogeneous samples.^{1,2} With the advent of third generation synchrotron sources and the rapid development in x-ray optics it is possible to obtain hard x-ray microprobes with (sub-)micrometer resolution. Most scanning microprobe techniques require thin slices or surfaces to be prepared of the sample to make the parts of interest available to the investigation. This is often destructive, difficult to achieve, and prone to change the element distribution under investigation.

X-ray fluorescence microtomography (XFEMT) takes advantage of the large penetration depth of hard x-rays in matter by combining the scanning microprobe with tomographic techniques. This allows to image the element distribution inside a sample on an arbitrary virtual section without the need of invasive sample preparation. This is particularly important for biological samples, such as the plant samples studied in this article. They have a delicate and complex structure that is very difficult to preserve. Therefore, it is important to reduce sample preparation to a minimum. So far, the samples have been shock frozen and freeze dried to stop the relocation of the elements by diffusion. We currently investigate the possibilities to use the method to investigate the transport mechanisms inside plants. So far, we have imaged the concentrations of physiologically relevant ions, trace elements, and heavy metal pollutants inside the plant samples at a cellular level.

Fluorescence tomography on larger samples with resolutions in the millimetre range was investigated earlier,³⁻⁵ pioneered by J. Hogan et al.³ The combination with x-ray microprobe techniques has only recently been implemented at the Synchrotron.⁶⁻⁹ A complementary method is differential absorption microtomography¹⁰ that uses the strong variations in photo absorption across an absorption edge of a particular element.

Fluorescence microtomography has been modeled by several groups,^{3-5,7,11,12} where L. Vincze et al.^{11,12} have given the most detailed description of the measurement process including multiple scattering effects and secondary fluorescence. So far, however, tomographic reconstruction techniques are all based on much simpler models that neglect multiple scattering, but take the attenuation of the incident and fluorescence radiation into account.^{4,5} For

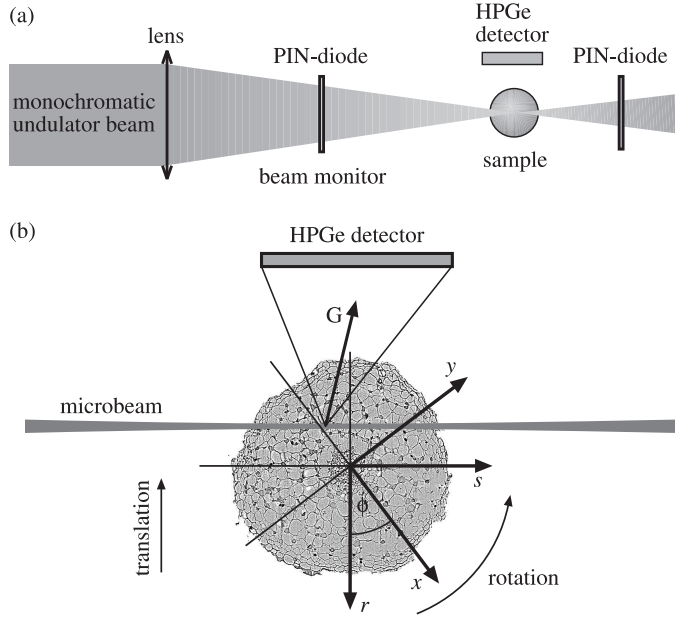


Figure 1. Experimental setup for x-ray fluorescence microtomography (XFEMT).

these reconstructions, the knowledge of the attenuation of the fluorescence radiation had to be assumed, despite the fact that it is not directly accessible by the experiment. Only recently, a self-consistent reconstruction technique was found that allows to reconstruct fluorescence tomograms including all attenuation effects without the prior knowledge of the attenuation inside the sample.¹³ This technique is described in section 4.

2. EXPERIMENTAL SETUP

Figure 1(a) depicts the XFEMT setup. Using an aluminium parabolic compound refractive lens,^{14,15} the undulator source is imaged onto the sample in a strongly focusing setup producing an intensive microbeam at the sample position. The undulator radiation is monochromatized by using either a Si 111 double crystal monochromator ($\Delta E/E \approx 10^{-4}$) or a band pass filter made of an absorber and a total reflexion mirror to single out a particular undulator harmonic ($\Delta E/E \approx 1\%$).¹⁶ With lateral extensions in the micro- and sub-micrometer range, the pencil beam produced this way is used to scan the sample in translation and rotation. The resulting x-ray fluorescence from the sample is recorded by an energy dispersive detector, e. g., a high purity germanium (HPGe) detector (see Figure 1) that is positioned at 90° with respect to the beam in the plane of the synchrotron. Taking advantage of the polarization of the synchrotron radiation, this avoids a flooding of the detector by scattered radiation (Compton and elastic scattering). A single tomographic projection is obtained by scanning the sample in r -direction (see Figure 1(b)) through the microbeam, recording in each step of the scan the full fluorescence spectrum. After each projection, the sample is rotated by an integer fraction of 360° and the next projection is recorded until the sample has undergone a full rotation. Two PIN-diodes, one in front of the sample and one behind it, are used to measure the intensity of the incident microbeam and the transmitted intensity, respectively.

3. MODELING THE EXPERIMENT

Following,^{3-5,7} we describe the measurement by a two dimensional model, accounting for absorption effects of the exciting beam and the fluorescence radiation inside the sample, but neglecting multiple scattering effects. The fluorescence intensity $I_{i\nu}(r, \phi)$ of the fluorescence line ν of the atomic species i at a given point (r, ϕ) of the scan is given by the generalized Radon transform (see Figure 1(b))

$$I_{i\nu}(r, \phi) = R_{\mu_{i\nu}} p_{i\nu}(x, y) = I_0 C_{\text{det}} \int ds f(\phi, r, s) \cdot p_{i\nu}(x(r, s), y(r, s)) \cdot g_{i\nu}(\phi, r, s), \quad (1)$$

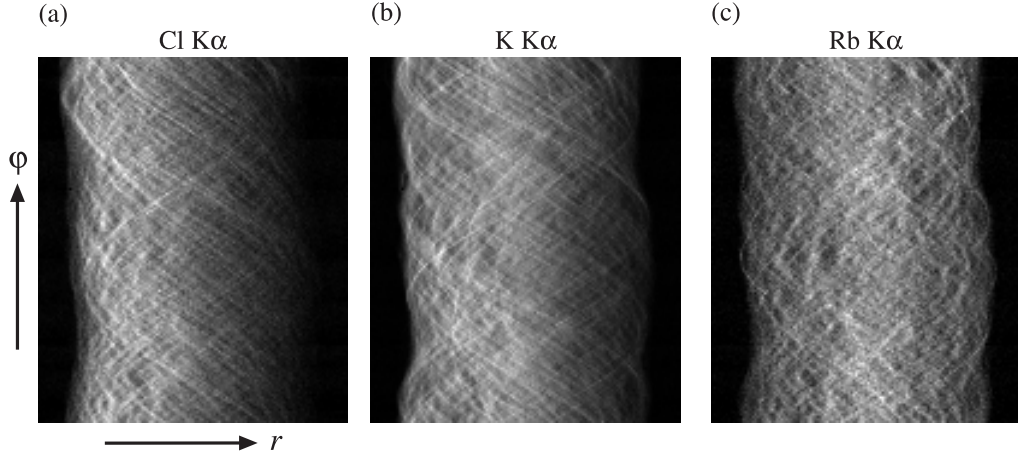


Figure 2. Fluorescence tomographic data from a root of the Mahogany plant (*Swietenia macrophylla*) for chlorine Kα ($E_{\text{Cl K}\alpha} = 2.62\text{keV}$) (a), potassium Kα ($E_{\text{K K}\alpha} = 3.31\text{keV}$) (b), and rubidium Kα ($E_{\text{Rb K}\alpha} = 13.38\text{keV}$) (c).

where I_0 is the intensity of the incident radiation, C_{det} describes the detector efficiency and the attenuation outside the sample and is considered independent of the scanning position (r, ϕ) . The fluorescence coefficient $p_{i\nu}(x, y)$ is proportional to the density $\rho_i(x, y)$ of the element under consideration. $f(\phi, r, s) = \exp(-\int_{-\infty}^s ds' \mu_0(r, s'))$ describes the attenuation of the incident ray up to the point (r, s) , where $\mu_0(x, y)$ is the distribution of the attenuation coefficient inside the sample at the incident energy E_0 . $g_{i\nu}(\phi, r, s) = \frac{1}{\Omega} \int_{\Omega} d\Omega \exp(-\int_G dt \mu_{i\nu}(x, y, z))$ accounts for the attenuation of the fluorescence radiation emitted into the solid angle Ω of the detector. The integral in the exponent in $g_{i\nu}(\phi, r, s)$ is taken along each ray G from (r, s) to the detector. $\mu_{i\nu}(x, y)$ is the distribution of the attenuation coefficient inside the sample at the energy $E_{i\nu}$ of the fluorescence line considered. $f(\phi, r, s)$ can be calculated by reconstructing $\mu_0(x, y)$ using the absorption data collected by the PIN-diodes. $g_{i\nu}$ is calculated from the distribution of the attenuation coefficients $\mu_{i\nu}$ inside the sample at the fluorescence energy. This data is not directly available from the experiment. It can be estimated by self-consistency considerations described in section 4.3.

4. TOMOGRAPHIC RECONSTRUCTION

4.1. Influence of Attenuation Inside the Sample

If all attenuation effects inside the sample are negligible, i. e., $f(\phi, r, s) = g_{i\nu}(\phi, r, s) = 1$ for all ϕ, s , and r in eq. (1), the standard Radon transform is obtained from eq. (1), and standard reconstruction techniques are applicable. Then, each feature in the sample yields the same contrast in all projections. In particular, the sinogram shows the symmetry $I_{i\nu}(-r, \pi + \phi) = I_{i\nu}(r, \phi)$ (the coordinate r has been chosen such that $r = 0$ corresponds to the rotation axis). This is illustrated in Fig. 2(c) that shows the Rb Kα fluorescence ($E_{\text{Rb K}\alpha} = 13.38\text{keV}$) from the root of the Mahogany plant that will be considered in more detail in section 5.1. The sinograms shown in Fig. 2 were recorded using a microbeam at $E = 19.5\text{keV}$ with a lateral extension of $6 \times 1.4\mu\text{m}^2$ horizontal by vertical full width at half maximum (FWHM).^{*} 152 projections were recorded over 360° using 128 step of $6\mu\text{m}$ to scan the sample horizontally. The symmetry in the Rb sinogram (Fig. 2(c)) shows that attenuation is negligible for the rubidium fluorescence line.

This is not the case for the Cl Kα and K Kα fluorescence lines shown in Fig. 2(a),(b), that display a decreasing intensity with increasing r . With the detector facing the sample from the left, the fluorescence that is emitted by the sample from points in the scan that are close to the detector is attenuated less than that emitted when the microbeam illuminates the sample at the far side of the detector. This asymmetry is caused by a non-trivial $g_{i\nu}(\phi, r, s)$ that is not directly accessible by the experiment. The bias in the sinogram, however, is a measure for the attenuation of the fluorescence inside the sample and can be used to estimate it and correct for it.

^{*}The numerical aperture of the refractive optics used to produce the microbeam is of the order 10^{-4} . Therefore, the depth of focus is about 4 orders of magnitude larger than its lateral extension and the lateral extension of the microbeam is constant over a sample of about 1mm in thickness.⁹

To obtain sufficient information for tomographic reconstruction from each part of the sample, it is important that the fluorescence radiation from that part can reach the detector with a sufficiently large number of counts from all perspectives, i. e., an angular interval that spans at least 180° . To assure this, it is favorable to acquire the tomographic projections over a full rotation rather than over 180° only.

To solve the fluorescence tomographic problem including attenuation correction, it is necessary to invert eq. (1) assuming the knowledge of both f and $g_{i\nu}$. This is done in the next section. In section 4.3, the bias in the sinogram is used to extract the attenuation of the fluorescence inside the sample.

4.2. Inverse Generalized Radon Transform for Known Attenuation

Assuming the knowledge of f and g , eq. (1) has been inverted by several groups.^{4,5} While T. Yuasa et al.⁴ use singular value decomposition solve the least square problem

$$\chi^2 = |R_{\mu_{i\nu}} p_{i\nu} - I_{i\nu}|^2 \stackrel{!}{=} \min. \quad (2)$$

to find the generalized inverse of (1), G.-F. Rust and J. Weigelt inverted (1) by algebraic iterative methods.⁵ We have implemented the generalized inverse by solving the χ^2 problem (2) by a conjugate gradient method. The method converges quickly in a few tens of iterations and can be applied to larger problems than the singular value decomposition.

In principle it is possible to measure the attenuation coefficient $\mu_{i\nu}$ for all fluorescence lines ($i\nu$) of interest by recording a transmission tomogram at each energy $E_{i\nu}$. With the knowledge of $\mu_{i\nu}$, the tomographic problem can be solved using the methods above. However, for a large number of fluorescence lines the additional measurement of transmission tomograms is time consuming and impractical, in particular since it requires the tomography setup to cover a large energy range (e. g., from about 2keV to several tens of keV).

4.3. Using Self-Consistency to Estimate the Attenuation Inside the Sample

With the correct distribution of the attenuation $\mu_{i\nu}$ at the fluorescence energy $E_{i\nu}$, the correct element distribution $p_{i\nu}$ can be found from the sinogram $I_{i\nu}$ using the conjugate gradient method (denoted by $R_{\mu_{i\nu}}^{-1}$) described in the last section. If the generalized radon transform $R_{\mu_{i\nu}}$ (eq. (1)) is applied to the reconstructed image, the sinogram $I_{i\nu}$ is recovered (up to measurement noise):

$$R_{\mu_{i\nu}} R_{\mu_{i\nu}}^{-1} I_{i\nu} = I_{i\nu} \quad (3)$$

If the attenuation $\mu_{i\nu}$ introduced in eq. (3) deviates from the correct attenuation, then eq. (3) is not fulfilled and the calculated sinogram on the left side of eq. (3) does not match the measured one $I_{i\nu}$. The discrepancy between the sinograms allows to quantify how well the attenuation $\mu_{i\nu}$ matches the correct attenuation in the experiment and is a self-consistency condition for the model eq. (1) used to describe the experiment. A measure for the deviation from the correct attenuation eq. (3) is

$$\chi_\mu^2 = |R_{\mu_{i\nu}} R_{\mu_{i\nu}}^{-1} I_{i\nu} - I_{i\nu}|^2, \quad (4)$$

that allows to formulate a non-linear least square problem for the unknown attenuation $\mu_{i\nu}$. We have solved this problem by conjugate gradients. This requires to calculate the derivative of χ_μ^2 with respect to $\mu_{i\nu}$ that involves taking a derivative of $R_{\mu_{i\nu}}^{-1}$ with respect to $\mu_{i\nu}$ that is not available in closed form. However, $\partial_{\mu_{i\nu}} \chi_\mu^2$ can be calculated from directional derivatives approximated by a difference quotient for a set of basis functions in $\mu_{i\nu}$ -space. If the same discretization is used for $\mu_{i\nu}$ as for $p_{i\nu}$, $\mu_{i\nu}$ typically lies in a 10^4 dimensional space. Calculating the directional derivatives in this high dimensional space is very time consuming and often not feasible. However, the effective dimensionality of the search space for $\mu_{i\nu}$ can be significantly reduced by physical considerations.

For a given energy E , the attenuation inside the sample is given by

$$\mu(E, x, y) = \sum_i \left(\frac{\mu}{\rho} \right)_i \rho_i(x, y), \quad (5)$$

where i labels all atomic species present in the sample, $(\mu/\rho)_i$ is the specific attenuation coefficient of the element i and $\rho_i(x, y)$ is its mass density distribution. For energies below 20keV, the attenuation by most elements (with

atomic number $Z > 5$) is dominated by photo absorption. Therefore, (μ/ρ) scales approximately like $E^{-\alpha}$ ($\alpha \approx 3$) for all elements away from their absorption edges. Thus,

$$\mu(E, x, y) = E^{-\alpha} \sum_i a_i \rho_i(x, y), \quad (6)$$

where a_i is an element specific constant. From eq. (6) it follows that the relative contribution of each element to the total attenuation is energy independent, unless the energy is varied across an absorption edge of a given atomic species i . In that case, a_i varies significantly.

To reconstruct the distributions of the atomic species of interest together with the attenuations at the fluorescence energies $E_{i\nu}$, we start with the reconstruction of the absorption tomogram measured in transmission at the energy E_0 of the microbeam. This yields the attenuation coefficient $\mu_0(x, y) = \mu(E_0, x, y)$ that can be used to calculate $f(\phi, r, s)$. As long as no absorption edge lies within the energy interval E and E_0 , the attenuation is proportional to $\mu_0(x, y)$ according to eq. (6).

In the next step, the element distributions are reconstructed starting with the most energetic fluorescence line $E_{i\nu}$. In most cases, the only absorption edges that lie between E_0 and $E_{i\nu}$ are those of the element i itself. In that case, $\mu_{i\nu}(x, y)$ is a linear combination of $\mu_0(x, y)$ and $p_{i\nu}(x, y)$. $p_{i\nu}$ is proportional to ρ_i and is a priori unknown. In the case where the absorption edges of more than one element in the sample lie above the highest fluorescence line, the search space for $\mu_{i\nu}$ must be extended to include the $p_{i\nu}$ of those elements. The distributions of these elements need to be reconstructed simultaneously as described below.

We start the reconstruction of the element distribution $p_{i\nu}(x, y)$ using μ_0 as the first search direction for $\mu_{i\nu}$ and find the minimum of (4) by line search. In a next iteration, the reconstructed $p_{i\nu}(x, y)$ is added to the search space for $\mu_{i\nu}$ and the gradient of χ_μ^2 is generated. Along this gradient direction χ_μ^2 is minimized by line search. The reconstructed $p_{i\nu}$ is added to the search space, the gradient is constructed and the search direction is generated using the conjugate gradient method by R. Fletcher and C. M. Reeves.¹⁷ The procedure is repeated until successive iterations do not significantly alter $\mu_{i\nu}$. The next element is reconstructed using μ_0 and the previously reconstructed $p_{i\nu}$ to span the initial search space for $\mu_{i\nu}$.

4.4. Reconstruction of a Numerical Test Sample

The reconstruction procedure described above was tested on numerically generated data. The numerical phantom used is shown in Fig. 3(a), assuming the Zn, Fe, and K distributions shown. The maximal concentrations were set to be $c_{\text{Zn}} \approx 1\%$, $c_{\text{Fe}} \approx 5\%$, and $c_{\text{K}} \approx 3\%$ as measured relative to the concentrations in the pure metallic solid, respectively. The concentrations were chosen such, that each of the elements has a significant contribution to the attenuation of the fluorescence radiation. In addition, a constant low Z matrix was assumed. It was modeled by an effective carbon concentration of $c_{\text{C}} \approx 60\%$ as measured relative to graphite. While the attenuation of this carbon matrix was taken into account to determine μ_0 and $\mu_{i\nu}$ shown in Fig. 3(b), its fluorescence signal is not accessible by the experiment, since the fluorescence lines of a low Z matrix lie in the soft x-ray regime (e. g., C $K\alpha = 277\text{eV}$). A pixel size of $5\mu\text{m}$ was assumed giving a field of view of $320\mu\text{m}$.

Using the concentrations given in Fig. 3(a) and the attenuations for the incident and the fluorescence radiation given in Fig. 3(b), the generalized Radon transform, eq. (1), was used to simulate the measurement process and generate the data (sinograms) shown in Fig. 3(c) that are composed of 91 projections over 360° with each spanning $320\mu\text{m}$ in $5\mu\text{m}$ steps. The incident energy was set to $E_0 = 20\text{keV}$ and the microbeam size was set to $5\mu\text{m}$. The transmission sinogram (first column in Fig. 3(c)) was generated using the standard radon transform. While the sinogram for this transmission data shows the full symmetry $I(r, \phi) = I(-r, \pi + \phi)$, the typical shadowing effects due to attenuation inside the sample are visible in the fluorescence sinograms, being the most pronounced for the K $K\alpha$ signal. To obtain sinograms that more realistically mimic the measurement process, poissonian noise was added to each pixel of the sinograms, assuming a maximum number of counts of 10000 in the brightest pixel.

For the reconstruction, only the data in row (c) of Fig. 3 was used. The reconstructions using standard tomographic techniques that neglect attenuation effects are shown in Fig. 3(d). For the transmission data in the first row, standard tomographic modeling is exact and the distribution of the attenuation coefficient μ_0 at the incident energy is recovered correctly. The reconstruction of the fluorescence data, however, underestimates and distorts the concentrations of the elements, which is particularly pronounced for potassium. While the concentrations of Zn and Fe are underestimated by 20% and 25%, respectively, the concentrations of potassium are underestimated by up

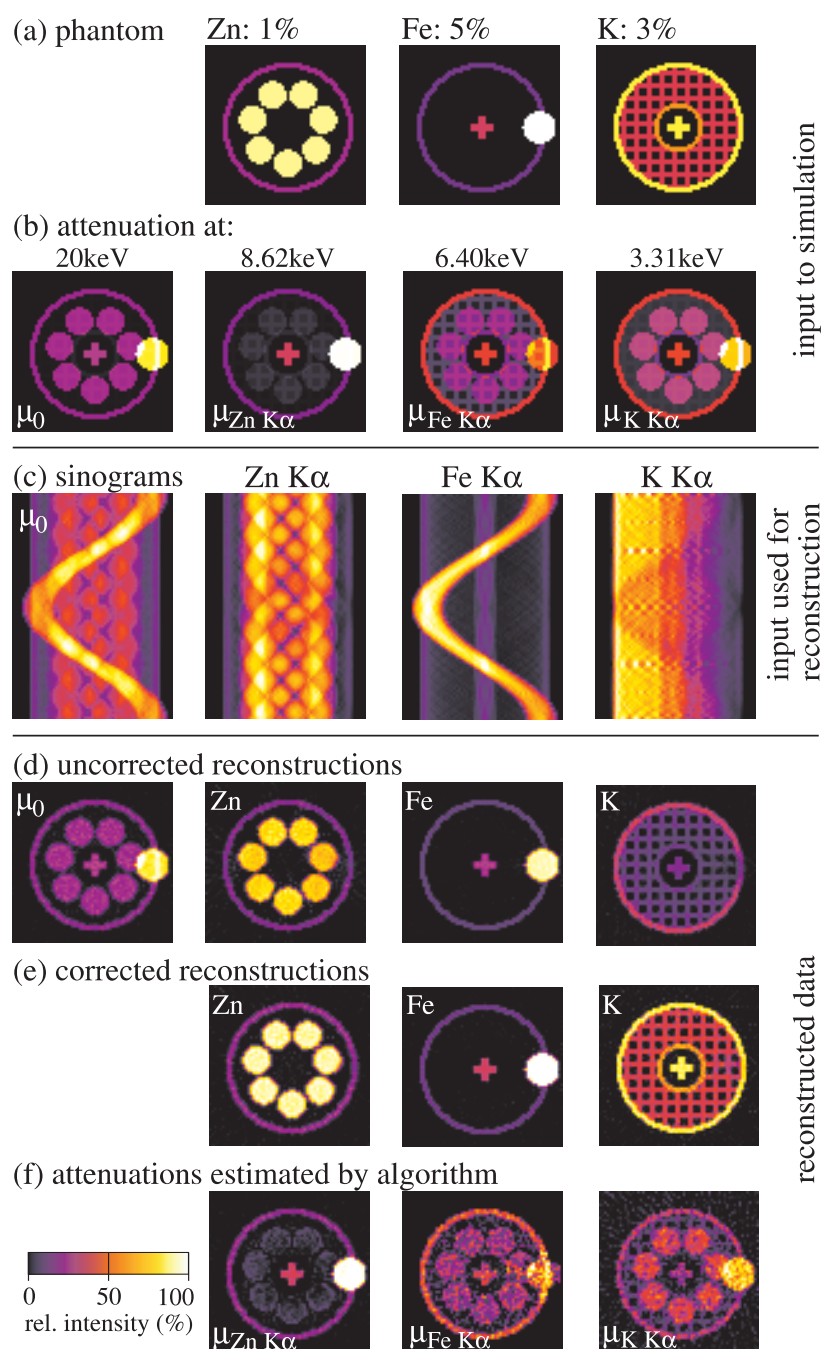


Figure 3. (a), (b) Numerical multi-element phantom that is used to generate a transmission sinogram at $E_0 = 20\text{keV}$ and three fluorescence sinograms (c). (d) Tomographic reconstruction neglecting attenuation effects. (e) Tomographic reconstruction with attenuation correction, yielding the reconstructed absorption (f). The relative intensity in each image is coded according to the gray scale given in (f). The scaling of the intensities in (a), (d), and (e) is the same for each column, as is the one for (b) and (f). (pixel size $5\mu\text{m}$, field of view $320\mu\text{m}$).

to a factor 5. In particular, the attenuation of the K signal in the vicinity of the high concentration of Fe is most pronounced. Besides the deficiency of properly reconstructing the element concentrations, no information about the attenuation inside the sample can be extracted from standard tomographic reconstruction.

Using the self-consistent reconstruction technique described in section 4.3, we obtain both the correct element distributions shown in Fig. 3(e) and an estimated attenuation for each fluorescence line (Fig. 3(f)). Comparing line (e) with (a) of Fig. 3 yields quantitative agreement upto noise and sampling induced variations below 5% for each pixel. The reconstructed attenuations are also in agreement with the input to the simulation (Fig. 3(b)).

5. RECONSTRUCTING THE CONCENTRATIONS INSIDE BIOLOGICAL SAMPLES

The following two plant samples were investigated during two user experiments at the European Synchrotron Radiation Facility (ESRF) in Grenoble, France.

5.1. Example 1: Root of the Mahogany Plant (*Swietenia macrophylla*)

The fluorescence microtomogram of this sample is used here to illustrate the reconstruction procedure described in the previous section. A detailed description of the experiment carried out at ID18 of the ESRF has been previously given.⁹ A monochromatic microbeam ($E = 19.5\text{keV}$) with lateral dimensions of $6\mu\text{m}$ horizontally and $1.4\mu\text{m}$ vertically was used to scan the sample with an incident flux above 10^{10} ph/s. The fluorescence radiation was recorded using a HPGe detector with an aperture of 7mm^2 positioned at 90° to and about 18mm away from the microbeam. 152 projections of 128 translational steps (step size $6\mu\text{m}$) were recorded over a full rotation. At each point, the fluorescence data was integrated over one second. The recorded sinograms for chlorine, potassium, and rubidium are shown in Fig. 2 and were discussed in section 4.1.

The attenuation corrected reconstruction is illustrated for the potassium $K\alpha$ signal, that shows a significant intensity bias in the sinogram as a consequence of attenuation of the fluorescence radiation. The sinogram used for the reconstruction is shown in Fig. 2(b). The reconstructed potassium distribution using the reconstruction scheme described in section 4 is shown in Fig. 4(a) on the left. The sinogram in the center is calculated according to $R_{\mu_{iv}} R_{\mu_{iv}}^{-1} I_{iv}$ using the self-consistently estimated attenuation shown on the right. The calculated sinogram (Fig. 4(a) (center)) is in agreement with the measured one (Fig. 2(b)) up to measurement noise, yielding a minimal χ_μ^2 in eq. (4). Fig. 4(b) on the other hand, shows the reconstructed distribution neglecting attenuation effects. A comparison with Fig. 4(a) shows that the concentrations are underestimated in particular in the center of the root. The resulting model sinogram $R_{\mu_{iv}} R_{\mu_{iv}}^{-1} I_{iv}$ is symmetric and does not match the measured data (Fig. 2(b)) very well, resulting in a large χ_μ^2 .

The attenuation corrected reconstructions for chlorine, potassium, and rubidium are shown in Fig. 5. Physiologically relevant ions, such as chlorine, potassium, and calcium were imaged, as well as the rubidium, that is about 0.003 times less concentrated than the potassium whose maximal concentration ranges around 100mMol/l . This illustrates the high sensitivity of the method that allows to investigate trace elements.

5.2. Example 2: Root of a Tomato Plant Grown on Heavy Metal Polluted Soil

This sample, a mycorrhizal root of the tomato plant, was investigated at ID22 of the ESRF using a microbeam with lateral dimensions of $3\mu\text{m}$ by $0.9\mu\text{m}$ (horizontal by vertical full width at half maximum). The microbeam was produced using an aluminium compound refractive lens with $N = 220$ single lenses with a focal distance of $f = 39\text{cm}$ using the full band width of an undulator harmonic peaked around 19.8keV .[†] The resulting flux in the microbeam was measured to $3.8 \cdot 10^9$ ph/s. To reduce scattering effects, the root was kept in a He atmosphere. It was scanned recording 132 projections with 105 horizontal translational steps of $1\mu\text{m}$ each, yielding a slight over sampling. The acquisition time was two seconds per step. The reconstructions for potassium, iron, and zinc using the full attenuation correction are shown in Fig. 6 together with the absorption tomogram at the incident energy. Details of the element distribution in single cells can be clearly resolved.

[†]This was achieved using a Mo foil ($250\mu\text{m}$ thickness) together with a Pd coated total reflexion mirror (reflexion angle 0.15°) to produce a band pass filter that removes from the undulator spectrum all but the one undulator harmonic at 19.8keV .

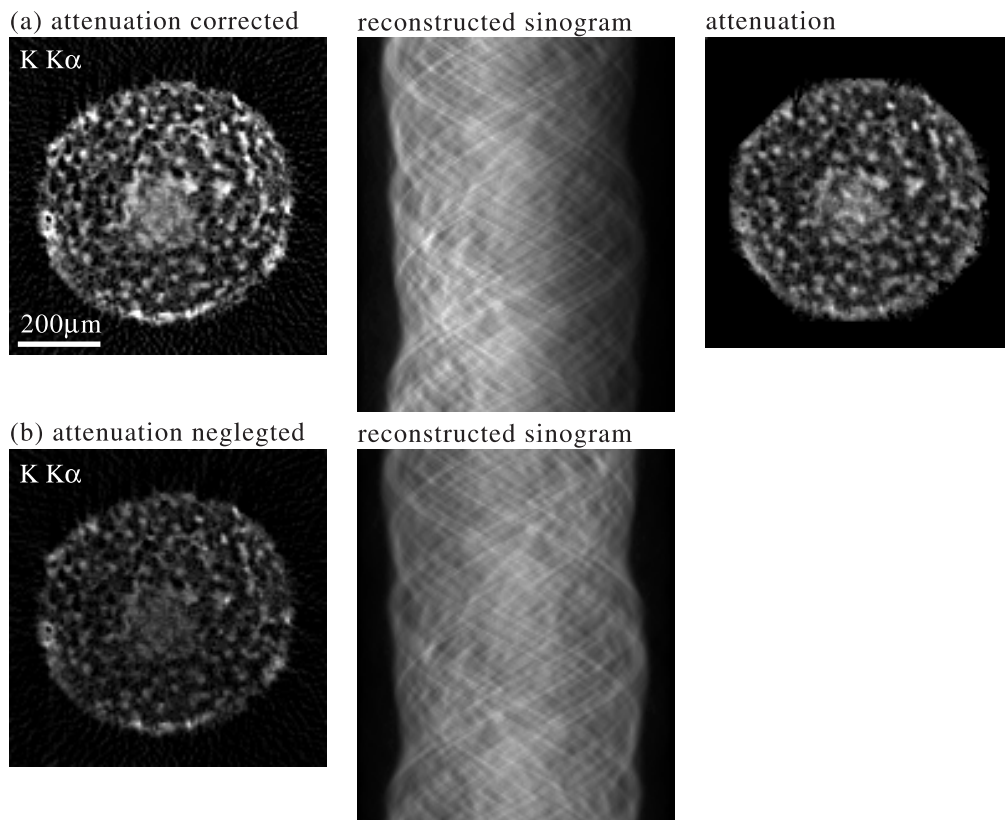


Figure 4. Reconstructed potassium distribution using the potassium $K\alpha$ sinogram shown in Fig. 2(b). (a) the self-consistent reconstruction scheme was used. Besides the reconstructed image (left), the sinogram $R_{\mu_{iv}} R_{\mu_{iv}}^{-1} I_{iv}$ (center) is calculated using the self-consistently determined attenuation shown on the right. (b) reconstruction neglecting attenuation. The model sinogram $R_{\mu_{iv}} R_{\mu_{iv}}^{-1} I_{iv}$ is symmetric.

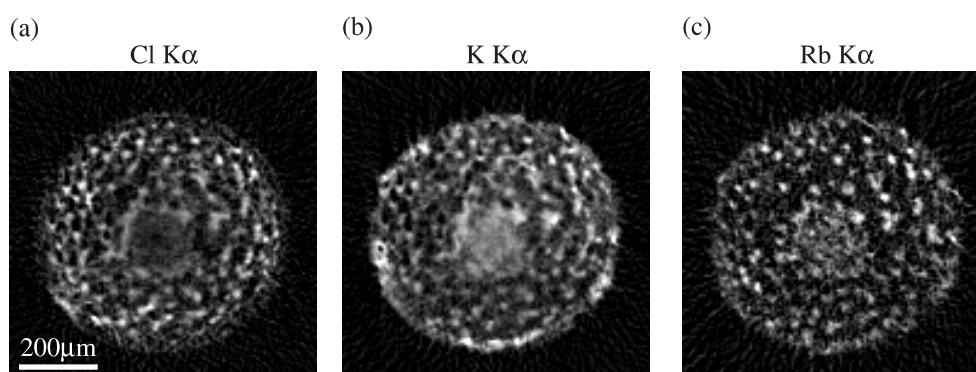


Figure 5. Reconstructed element distributions for (a) chlorine, (b) potassium, and (c) rubidium on a cross section through the root of the Mahogany plant.

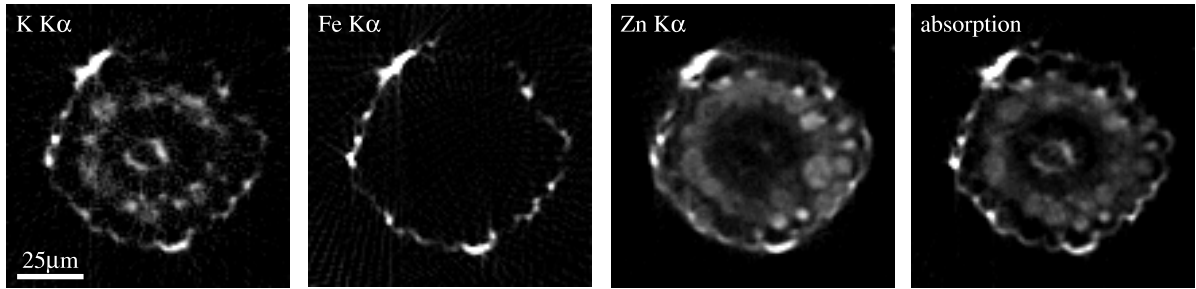


Figure 6. Virtual section across a mycorrhizal root of a tomato plant grown on heavy metal polluted soil. The distributions of potassium, iron, and zinc are shown together with the attenuation coefficient μ_0 at the incident energy reconstructed from the transmission data.

6. CONCLUSION AND OUTLOOK

X-ray fluorescence microtomography (XFEMT) allows to image the element distributions on an arbitrary virtual section through a sample with resolutions in the micrometer range. For high Z elements, the method is very sensitive. The size of samples that can be investigated is limited by the attenuation of the fluorescence radiation of the elements of interest. The low Z matrix of most biological samples has a favorably low absorption making the method particularly useful for their investigation. An major advantage of the method is the reduced amount of sample preparation required to obtain the element distribution.

To establish the method as an efficient standard technique, the acquisition time for a tomogram needs to be reduced significantly. The major problem to be solved to achieve this is to overcome the limited count rate capability of the detector system. Here, wave length dispersive detectors might be a solution.⁶ To increase the flux in the microbeam, more efficient microbeam optics can be used in the future. Using refractive lenses made of more transparent materials, such as beryllium, the flux in the microbeam could be increased by almost two orders of magnitude. Reduced acquisition time would allow to scan the sample three dimensionally. In principle, other x-ray analytical methods can also be combined with scanning microtomographic techniques.

ACKNOWLEDGMENTS

The experiments were carried out under the user proposals LS-1422 and LS-1739 at the ESRF in Grenoble. We would like to thank R. Ruffer and his team for their support at beamline ID18 and J.-M. Rigal for his help at beamline ID22. The *Swietenia macrophylla* sample was provided by G. Noldt, Ordinariat für Holzbiologie, University of Hamburg, Germany.

REFERENCES

1. M. Labrenz, G. K. Druschel, T. Thomsen-Ebert, B. Gilbert, S. A. Welch, K. M. Kemner, G. A. Logan, R. E. Summons, G. De Stasio, P. L. Bond, B. Lai, S. D. Kelly, and J. F. Banfield, "Formation of sphalerite (ZnS) deposits in natural biofilms of sulfate-reducing bacteria," *Science* **290**, pp. 1744–1747, 2000.
2. S. Bohic, A. Simionovici, A. Snigirev, R. Ortega, G. Devès, D. Heymann, and C. G. Schroer, "Synchrotron hard x-ray microprobe: Fluorescence imaging of single cells," *Appl. Phys. Lett.* **78**, 2001.
3. J. P. Hogan, R. A. Gonsalves, and A. S. Krieger, "Fluorescent computer tomography: A model for correction of x-ray absorption," *IEEE Trans. Nucl. Sci.* **38**(6), pp. 1721–1727, 1991.
4. T. Yuasa, M. Akiba, T. Takeda, M. Kazama, A. Hoshino, Y. Watanabe, K. Hyodo, F. A. Dilmanian, T. Akatsuka, and Y. Itai, "Reconstruction method for fluorescent x-ray computed tomography by least-squares method using singular value decomposition," *IEEE Trans. Nucl. Sci.* **44**(1), pp. 54–62, 1997.
5. G.-F. Rust and J. Weigelt, "X-ray fluorescent computer tomography with synchrotron radiation," *IEEE Trans. Nucl. Sci.* **45**(1), pp. 75–88, 1998.
6. M. Nagedolfeizi, J.-S. Chung, G. E. Ice, W. B. Yun, Z. Cai, and B. Lai, "X-ray fluorescence microtomography on a SiC nuclear fuel shell," in *Materials Research Society Symposium Proceedings*, vol. 524, p. 233, 1998.

7. A. Simionovici, M. Chukalina, M. Drakopoulos, I. Snigireva, A. Snigirev, C. Schroer, B. Lengeler, K. Janssens, and F. Adams, "X-ray fluorescence microtomography: experiment and reconstruction," in *Developments in X-ray Tomography II*, U. Bonse, ed., vol. 3772 of *Proceedings of the SPIE*, pp. 328–337, SPIE, (Bellingham), 1999.
8. A. S. Simionovici, M. Chukalina, C. Schroer, M. Drakopoulos, A. Snigirev, I. Snigireva, B. Lengeler, K. Janssens, and F. Adams, "High-resolution x-ray fluorescence microtomography of homogeneous samples," *IEEE Trans. Nucl. Sci.* **47**(6), pp. 2736–2740, 2000.
9. C. G. Schroer, J. Tümmeler, T. F. Günzler, B. Lengeler, W. H. Schröder, A. J. Kuhn, A. S. Simionovici, A. Snigirev, and I. Snigireva, "Fluorescence microtomography: External mapping of elements inside biological samples," in *Penetrating Radiation Systems and Applications II*, F. P. Doty, H. B. Barber, H. Roehrig, and E. J. Morton, eds., vol. 4142 of *Proceedings of the SPIE*, pp. 287–296, SPIE, (Bellingham), 2000.
10. U. Bonse, H. Johnson, M. Nichols, R. Nußhardt, S. Krasnicki, and J. Kinney, "High resolution tomography with chemical specificity," *Nucl. Instrum. Methods A* **246**, pp. 644–648, 1986.
11. L. Vincze, K. Janssens, B. Vekemans, and F. Adams, "Monte Carlo simulation of x-ray fluorescence spectra: Part 4. photon scattering at high x-ray energies," *Spectrochim. Acta, Part B* **54**, pp. 1711–1722, 1999.
12. L. Vincze, K. Janssens, B. Vekemans, and F. Adams, "Monte Carlo simulation of x-ray fluorescence and scattering tomography experiments," in *Developments in X-ray Tomography II*, U. Bonse, ed., vol. 3772 of *Proceedings of the SPIE*, pp. 328–337, SPIE, (Bellingham), 1999.
13. C. G. Schroer, "Reconstructing x-ray fluorescence microtomograms," *Appl. Phys. Lett.* , 2001. To be published.
14. B. Lengeler, C. G. Schroer, M. Richwin, J. Tümmeler, M. Drakopoulos, A. Snigirev, and I. Snigireva, "A microscope for hard x-rays based on parabolic compound refractive lenses," *Appl. Phys. Lett.* **74**(26), pp. 3924–3926, 1999.
15. B. Lengeler, C. Schroer, J. Tümmeler, B. Benner, M. Richwin, A. Snigirev, I. Snigireva, and M. Drakopoulos, "Imaging by parabolic refractive lenses in the hard x-ray range," *J. Synchrotron Rad.* **6**, pp. 1153–1167, 1999.
16. C. G. Schroer, B. Lengeler, B. Benner, T. F. Günzler, M. Kuhlmann, A. S. Simionovici, S. Bohic, M. Drakopoulos, A. Snigirev, I. Snigireva, and W. H. Schröder, "Microbeam production using compound refractive lenses: beam characterization and applications," in *X-Ray Micro- and Nano-Focusing: Applications and Techniques II*, I. McNulty, ed., vol. 4499 of *Proceedings of the SPIE*, 2001. To be published.
17. R. Fletcher and C. M. Reeves, "Function minimization by conjugate gradients," *Computer J.* **7**, pp. 149–154, 1964.